The Journal of Chemical Physics

Spectroscopic signatures of states in the continuum characterized by a joint experimental and theoretical study of pyrrole

Cite as: J. Chem. Phys. **157**, 204305 (2022); https://doi.org/10.1063/5.0123603
Submitted: 31 August 2022 • Accepted: 04 November 2022 • Accepted Manuscript Online: 04 November 2022 • Published Online: 22 November 2022

Madhubani Mukherjee, T. P. Ragesh Kumar, Miloš Ranković, et al.

AIP Publishing

The Journal of Chemical Physics ARTICLE scitation.org/journal/jcp

Spectroscopic signatures of states in the continuum characterized by a joint experimental and theoretical study of pyrrole

Cite as: J. Chem. Phys. 157, 204305 (2022); doi: 10.1063/5.0123603
Submitted: 31 August 2022 • Accepted: 4 November 2022 •
Published Online: 22 November 2022

Madhubani Mukherjee,[1] T. P. Ragesh Kumar,[2] Miloš Ranković,[2] Pamir Nag,[2] Juraj Fedor,[2,a)] and Anna I. Krylov[1,a)]

AFFILIATIONS

[1] Department of Chemistry, University of Southern California, Los Angeles, California 90089, USA
[2] J. Heyrovský Institute of Physical Chemistry, Czech Academy of Sciences, Dolejškova 3, 18223 Prague 8, Czech Republic

[a)] **Authors to whom correspondence should be addressed:** juraj.fedor@jh-inst.cas.cz and krylov@usc.edu

ABSTRACT

We report a combined experimental and theoretical investigation of electron–molecule interactions using pyrrole as a model system. Experimental two-dimensional electron energy loss spectra (EELS) encode information about the vibrational states of the molecule as well as the position and structure of electronic resonances. The calculations using complex-valued extensions of equation-of-motion coupled-cluster theory (based on non-Hermitian quantum mechanics) facilitate the assignment of all major EELS features. We confirm the two previously described π resonances at about 2.5 and 3.5 eV (the calculations place these two states at 2.92 and 3.53 eV vertically and 2.63 and 3.27 eV adiabatically). The calculations also predict a low-lying resonance at 0.46 eV, which has a mixed character—of a dipole-bound state and σ^* type. This resonance becomes stabilized at one quanta of the NH excitation, giving rise to the sharp feature at 0.9 eV in the corresponding EELS. Calculations of Franck–Condon factors explain the observed variations in the vibrational excitation patterns. The ability of theory to describe EELS provides a concrete illustration of the utility of non-Hermitian quantum chemistry, which extends such important concepts as potential energy surfaces and molecular orbitals to states embedded in the continuum.

I. INTRODUCTION

Processes induced by collisions of electrons with molecules play an important role in various high-energy environments, such as plasmas. They are ubiquitous in interstellar and atmospheric media, fusion and plasma reactors, and hypersonic propulsion.[1] Electron-induced processes are also important in the condensed phase, e.g., when high-energy radiation can produce free electrons (as in the radiolysis of water), plasmonic catalysis (when chemistry is initiated by electrons generated by plasmon excitations[2]), and plasma electrochemistry.[3]

Electron collision with a molecule below the ionization threshold can lead to three possible outcomes: elastic scattering, inelastic scattering, in which the energy of an electron is partially transferred to molecular vibrations or rotations, and electron attachment producing bound or transient molecular anions. Electron scattering at relatively low electron energies is non-reactive, leading to vibrationally excited (hot) molecules. In contrast, electron trapping by a molecular target can initiate chemical reactions, e.g., isomerization or even dissociation. Chemical transformations become possible because electron attachment changes the electronic configuration of the molecule, altering its bonding pattern—for example, electron attachment to the anti-bonding molecular orbitals can lead to bond-breaking in a process called dissociative electron attachment (DEA).[4–7] Because of the changes in the electronic state of the molecule, DEA can lead to the breaking of chemical bonds by relatively cold electrons—for example, electrons with about 2 eV of kinetic energy have been shown to be effective in breaking chemical bonds (~5 eV) in double-stranded DNA.[8,9] DEA induced by vibrationally cold plasma with hot electrons is used for removing pollutants in various industrial applications.[10,11]

Therefore, a fundamental understanding of the processes induced by electron–molecule interactions is essential for various applications using plasma (plasma chemistry, electron lithography, chemical vapor deposition, etc.), hypersonic propulsion, fusion reactors, radiation science, planetary science, and astrophysics. Predictive theoretical modeling of these processes is challenging because of the need to deal with the many-body molecular problem and continuum free-electron states. Particularly difficult is the theoretical treatment of electronic resonances—transient states produced by electron capture that have a finite lifetime and decay by autoionization. In electron–molecule scattering, resonances affect scattering cross-sections, change the vibrational excitation pattern, and can lead to reactive processes such as DEA.

In Hermitian quantum mechanics, resonances are embedded in the continuum part of the spectra and correspond to the increased density of states at certain energies. One can avoid the inconveniences of dealing with the continuum by invoking non-Hermitian quantum mechanics approaches[12–15] in which the problem is reformulated such that resonances become isolated states with L^2-integrable wavefunctions and complex energies. These ideas were exploited in recent theoretical developments that extended standard quantum chemistry approaches, such as equation-of-motion coupled-cluster (EOM-CC),[16–18] symmetry-adapted cluster configuration interaction (SAC-CI),[19,20] and algebraic diagrammatic construction[21] theories, to treating electronic resonances.[15,22]

In this contribution, we report experimental results for electron scattering from pyrrole using two-dimensional electron energy loss spectroscopy (EELS). In these experiments,[23,24] electrons of different incident energies are scattered from molecular targets, and the energy of the scattered electrons is recorded, thus allowing one to obtain the probability of energy loss as a function of the incident electron energy. The EELS report on the vibrational excitations of the molecule via direct (non-resonant) and indirect (via resonances) scattering.

To interpret the experimental EELS, we employ high-level quantum chemistry methods to describe molecular electronic structure. In particular, we compute resonances using EOM-CC methods[16–18] augmented with the complex absorbing potential (CAP)[15,25–27] as well as EOM-CC with complex basis functions (CBF).[28–30]

To describe non-resonant vibrational excitations, we use the theoretical approach of Itikawa,[31] in which molecule–electron interactions are approximated by a long-range electrostatic potential. To compute vibrational excitation via resonances, we use a Franck–Condon-based (i.e., projection) approach, treating the vibrational excitation in the same way as in photodetachment. The details of the theoretical framework are given below.

Pyrrole is a simple organic molecule from the class of heteronuclear aromatic compounds such as indole, imidazole, and nucleobases. We use it as a model system to study electron-induced chemistry in small aromatic molecules. Pyrrole's rich photochemistry[32] is suggestive of similarly interesting electron-induced chemistry. As many other closed-shell conjugate organic molecules, pyrrole is not expected to support bound anions, at least not at its equilibrium structure, but electronic resonances. The spectroscopic signatures of resonances were observed by Modelli and Burrow,[33] who reported the electron transmission (ET) spectra of pyrrole. They found two peaks in the ET spectra, which they assigned to two π resonances. The assignment was supported by quantum-chemistry estimates of vertical attachment energy using MP2 and DFT. Later, De Oliveira *et al.*[34] carried out scattering calculations with the Schwinger multichannel (SMC) method, confirming the presence of the two π resonances and also reporting two high-lying σ^* resonances. Note that no evidence of the σ^* resonances was observed in the original ET experiments.[33] A more recent ET experiments[35] confirmed the previous assignments and additionally reported a sharp feature around 0.5 eV, which was attributed to a vibrational Feshbach resonance (along the NH stretching mode) due to a putative virtual state. Table S1 in the supplementary material shows resonance peak positions reported in the previous studies.[33–35]

The interest in the putative σ^* resonance stems from its anticipated role in the DEA processes, in analogy to the proposed mechanism for double-strand breaking by electrons in DNA,[8,9] according to which[4–7] the capture of the electron proceeds via a π-type resonance that undergoes a non-adiabatic transition to a σ^*-type resonance, leading to eventual bond-breaking. The experimental footprints of such π^*-to-σ^* transitions have been reported for several unsaturated organic molecules.[36–42] Recently, calculations of DEA in C_2H have revealed a similar interplay between π- and σ-type resonances.[43]

The structure of the paper is as follows: Sec. II describes our theoretical framework. Sections IV and III provide details of the experimental setup and calculations. The results are presented and discussed in Sec. V. Additional details are provided in the supplementary material.

II. THEORETICAL FRAMEWORK

Pyrrole is a planar, closed-shell aromatic molecule of C_{2v} symmetry. Its ground state can be well described by standard quantum-chemistry methods such as coupled-cluster (CC) or density functional theory (DFT). To describe electron-attached states, we use the EOM-CC method[16,18] for electron-attached states (EOM-EA-CC), in which target states are described by electron-attaching operators acting on the ground-state CC wave function. At the CCSD level (CC with single and double substitutions), this leads to

$$|\Psi\rangle = \left(\sum_a r^a a^\dagger + \frac{1}{2}\sum_{abi} r_i^{ab} a^\dagger b^\dagger i\right) e^{\hat{T}_1+\hat{T}_2}|\Phi_0\rangle, \tag{1}$$

where $p^\dagger$ and q denote creation and annihilation operators corresponding to orbitals ϕ_p and ϕ_q, respectively, and Φ_0 is the reference determinant of the neutral state (following the standard notations, letters $a, b, c, \ldots$ denote virtual orbitals with respect to Φ_0 and $i, j, k, \ldots$ denote orbitals occupied in Φ_0). The amplitudes of cluster operators $\hat{T}_1$ and $\hat{T}_2$ are found by solving CCSD equations for the reference state and the amplitudes of EOM operators r are found by diagonalizing the similarity-transformed Hamiltonian, $\overline{H} = e^{-\hat{T}}\hat{H}e^{\hat{T}}$.

To describe states in the continuum (resonances), we use the EOM-CC method augmented with CAP,[15,22]

$$\hat{H}(\eta) = \hat{H}_0 - i\eta\hat{W}(r), \tag{2}$$

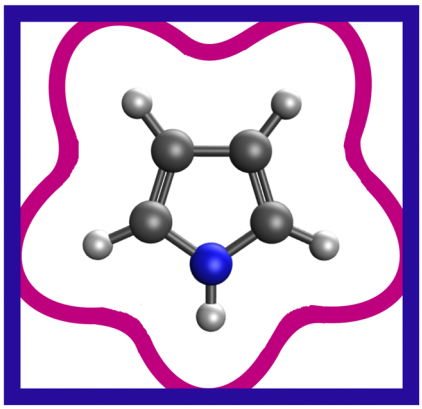

FIG. 1. Onsets for box-CAP (purple) and Voronoi-CAP (magenta). At the equilibrium geometry of neutral pyrrole, the onsets of the box-CAP are 6.28 Å (X), 2.67 Å (Y), and 6.25 Å (Z) from the molecular center of mass, and the onset for the shown Voronoi-CAP is 4.13 Å from the atomic centers (additional Voronoi-CAP calculations used a tighter onset of 3.00 Å, which matches better the onset of the box-CAP in the Y-direction).

where $\hat{H}_0$ is the original molecular Hamiltonian, η is the parameter controlling the strength of the CAP, and $\hat{W}(r)$ is an artificial absorbing potential (usually quadratic).[25–27] Adding pure imaginary potential to the Hamiltonian converts resonances into isolated states with L^2-integrable wavefunctions. We used two types of CAPs that differ by their shape: box-CAP and Voronoi-CAP[44] shown in Fig. 1. Both CAPs are zero in the molecular region and rise quadratically after a certain onset value (see the supplementary material for details).

To mitigate the perturbation introduced by the finite-strength CAP on the energy in the finite basis set, one needs to find[25–27] the optimal value of CAP strength η, which is done by calculating the η-trajectory and finding the minimum of $\eta\frac{dE}{d\eta}$ with respect to η. The error can be further reduced by applying a perturbative correction[26,45,46] to the energy, such as

$$U(\eta) = E(\eta) - \eta\frac{dE}{d\eta}, \tag{3}$$

and computing the optimal η from the first-order corrected trajectory. Below, we refer to the results obtained with and without correction as the first (first) and zero (zeroth) order values, respectively.

To further test the results of the calculations for robustness, we also carried out EOM-EA-CCSD calculations with CBF[28–30]—an alternative approach to treating resonances based on complex-scaling formalism.[12,47] In these calculations, one uses complex exponents for the most diffuse functions,[28,48] which are formally equivalent to the exterior complex scaling.[49]

A. Calculations of EELS

To compute EELS, we distinguish two regimes of electron scattering—direct and via resonances. The theory for computing cross-sections for vibrational excitations of molecules by electron impact has been succinctly summarized by Itikawa.[31] The cross-sections are derived using scattering theory and applying several approximations: the Born approximation to the scattering problem, fixed nuclei (no vibrational motion of the target), and sudden vibrational excitation. The molecule–electron interaction is described by the multipolar expansion of the long-range electrostatic potential. When only the leading dipole term is retained, the expression for the integral cross-section (ICS) for electron-impact vibrational excitation becomes

$$Q(n_0 \to n') = \frac{8\pi}{3}\frac{1}{k_0^2}\ln\left|\frac{k_0 + k_{n'}}{k_0 - k_{n'}}\right| \sum_{\alpha=x,y,z} \left|\langle n'|\hat{\mu}_\alpha|n_0\rangle\right|^2, \tag{4}$$

where n_0 and n' denote the initial and final vibrational states of the neutral molecule, k_0 and k_n denote the momenta of the incident and scattered electrons related to their kinetic energy via $E_k = \frac{k^2}{2}$, and $\langle n'|\hat{\mu}_\alpha|n_0\rangle$ is the matrix element of the dipole operator. The same dipole matrix element[31] enters the expression for the intensity of the IR transitions,

$$A(n_0 \to n') = \frac{2\pi\omega}{3\hbar c} \sum_{\alpha=x,y,z} \left|\langle n'|\hat{\mu}_\alpha|n_0\rangle\right|^2, \tag{5}$$

where ω is the frequency of the transition. Thus, one can easily extract $\sum_{\alpha=x,y,z}\left|\langle n'|\hat{\mu}_\alpha|n_0\rangle\right|^2$ from the IR intensities (either experimental or computed) and use them to compute electron impact excitation cross-sections Q via Eq. (4). Here, we use scaled computed harmonic vibrational frequencies of neutral pyrrole computed by DFT (details below). To circumvent potential problems with unit conversion, we did not carry out intensity rescaling (as per Ref. 31), but instead used vibrational dipole moments as reported by the frequency calculation.

By virtue of Eq. (4), only IR-active modes can be excited by electron impact; hence, non-resonant EELS is expected to resemble the IR spectrum but with renormalized intensities. Note that, within the harmonic approximation, only fundamental vibrational transitions can be excited. Equation (4) also shows that the cross-sections decay with the increasing energy of incoming electrons, with the intensities of low-energy loss peaks decaying faster than high-energy loss peaks, so that the relative intensities of the EELS peaks change with energy.

When the energy of an incident electron matches the position of an electronic resonance, it can be trapped in this state, which increases the probability of inelastic scattering and changes the mechanism of vibrational excitation. Hence, the resonances are revealed by increasing intensities in EELS. The pattern of the resulting vibrational excitation can report on the structure of the resonant state in the same way that photodetachment spectra report on structural differences between anionic and neutral species.[50] In fact, one can think of the electron scattering via resonances as a reverse process of photodetachment so that the probabilities to excite specific vibrations are given by the Frank–Condon factors (FCFs),

$$P(n_{i,0} \to n_f') \sim \left|\langle n_{i0}|n_f'\rangle\right|^2, \tag{6}$$

where indices i and f refer to the initial and final electronic states (here, the resonance and the neutral, respectively). Within the harmonic approximation, the non-diagonal FCFs (e.g., transitions in which the initial and final vibrational states are not the same) are

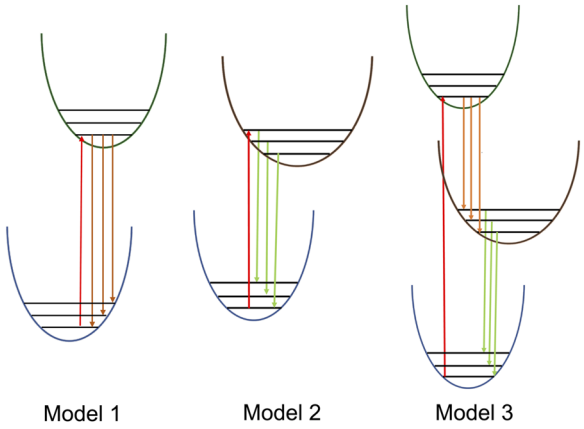

FIG. 2. Calculations of vibrational excitation via resonances. Model 1: Direct scattering via the 00 level of a resonance; Model 2: scattering at energies exceeding the resonance position via vibrationally hot resonance; Model 3: Scattering via a non-adiabatic transition to a lower resonance.

allowed for the vibrational modes along which the shape of the potential energy surface is different for the two electronic states. Because the diagonal transitions correspond to zero energy loss, the new features due to resonances appear only for the normal modes along which either the structure (i.e., r_e) or the curvature of the potential energy surface (PES) changes.

To model the vibrational excitation via resonances, we consider several models:

1. Direct process via the lowest vibrational state; in this case, the EELS is computed as FCFs for the transition from the lowest vibrational state of the resonance to the neutral target state. This description is appropriate when the incident energy matches exactly the 00 transition energy between the neutral state and the resonance.
2. Scattering at incident energies above the resonance: in this case, we consider a vibrationally hot resonance state and scale the FCF intensities accordingly. We consider two limiting cases: when the excess energy is thermalized (and the vibrational levels are populated according to the Boltzmann populations) and when no thermalization occurs so that all accessible excited vibrational levels are equally populated.
3. Process involving two resonance states: we assume that a higher resonance state is populated first, followed by the fast non-adiabatic transition to the vibrationally hot lower state and subsequent detachment.

The three models are summarized in Fig. 2. More details are given in Section III and in the supplementary material.

III. COMPUTATIONAL DETAILS

The resonances were computed using the CAP-EOM-EA-CCSD method. We computed the vertical and adiabatic positions of resonances and also performed scans of the PES along the N–H bond stretching. We identified four resonances—one in each symmetry block. We found no other resonances up to 8 eV. Throughout this paper, we use Q-Chem's symmetry notations,[51] which differ from the standard notations[52] for some point groups (including C_{2v}).

Vertical positions of resonances were computed at the equilibrium geometry of neutral pyrrole optimized with CCSD/aug-cc-pVTZ.

CAP-EOM-EA-CCSD calculations were carried out using the aug-cc-pVDZ basis, augmented by additional even-tempered *s* and *p* functions on each atom, following the protocol from our previous studies.[43,45,46,53] The exponents of the first additional basis functions of each type were: α(N,s) = 0.030 62, α(N,p) = 0.028 055, α(C,s) = 0.023 45, α(C,p) = 0.020 205, α(H,s) = 0.014 87, α(H,p) = 0.141, and the subsequent exponents were divided by 2. We considered aug-cc-pVDZ+2*s*2*p*, aug-cc-pVDZ+3*s*2*p*, aug-cc-pVDZ+4*s*2*p*, aug-cc-pVDZ+4*s*3*p*, aug-cc-pVDZ+5*s*3*p* with pure imaginary box and Voronoi CAPs. To investigate the basis set effects further, we also carried out calculations (box-CAP) with aug-cc-pVTZ+3*s*3*p*; in these calculations, the exponents of the first additional basis functions of each type were: α(N,s) = 0.0576, α(N,p) = 0.0491, α(C,s) = 0.044 02, α(C,p) = 0.035 69, α(H,s) = 0.025 26, α(H,p) = 0.102.

The CBF calculations[29,30] were carried out with EOM-EA-CCSD and the aug-cc-pVDZ+2*s*2*p* and aug-cc-pVDZ+4*s*2*p* basis sets in which the exponents of the additional Gaussian diffuse functions were scaled by the complex number $e^{-2i\theta}$, with θ varying from 0° to 35° in intervals of 1°.

To compute adiabatic positions of the resonances, we optimized their structures using analytic gradients for CAP-EOM-CCSD developed by Benda and Jagau.[54,55] The $^2A_1$, $^2A_2$, and $^2B_2$ resonances were optimized using pure imaginary box-CAP with the aug-cc-pVDZ+4*s*3*p* basis as follows: First, the equilibrium geometry of the neutral molecule was taken, and with the same CAP onsets and the optimum η parameter, the geometry was optimized. At the new geometry, the onsets were computed for the neutral molecule using the same criterion. The η_{opt} value was found at the updated CAP onsets and optimized geometry. These iterations were continued until the values of the onsets and η_{opt} converged. Using the same protocol and algorithm as Benda and Jagau,[55] we computed the minimum energy crossing point (MECP) between the σ^*-resonance and the ground state of neutral pyrrole. The scans of the PES of the four resonances were carried out with the aug-cc-pVDZ+4*s*3*p* basis set and box-CAP starting from the neutral geometry by elongating the N–H bond (planar C_{2v} structures).

To compute FCFs, one needs frequencies in addition to the optimized geometries. Because analytic second derivatives are not yet available for CAP-EOM-CCSD, such calculations can only be carried out using finite differences (of the first derivatives) with symmetry turned off. This makes the calculations considerably more expensive, especially for higher-lying resonances. Therefore, we were only able to compute CAP-EOM-CCSD frequencies for the lowest resonance ($^2A_1$). In these calculations, we used CAP-EA-EOM-CCSD/aug-cc-pVDZ+2*s*2*p* with the converged values of the onset. We tested the sensitivity of the computed frequencies to the CAP onset by varying the onsets by ±1 bohr. We found that the frequencies are rather insensitive, showing an average change in the absolute relative values of about 0.10–0.12 (see Table S17 in the supplementary material).

To obtain the frequencies of the two π resonances ($^2B_2$ and $^2A_2$), we first optimized their geometries with ωB97X-D/6-311++G** fixing the orbital occupation such that the attached

electron resides on the orbital of a proper symmetry and shape using the maximum overlap method.[56] These structures (shown in the supplementary material) agree reasonably well with the CAP-EOM-EA-CCSD structures. We then used the same method to compute the respective frequencies.

A. Calculations of the non-resonant EELS

We simulated the non-resonant EELS at incident energies up to 4.0 eV. We used frequencies and intensities computed using the ωB97X-D/6-311++G** at the corresponding optimized geometry. The summary of frequencies and normal modes is given in Fig. S14 in the supplementary material. We also computed the frequencies with RI-MP2/aug-cc-pVTZ and found that the differences between the two sets of frequencies and intensities are insignificant (see Fig. S15 in the supplementary material for a comparison). Figure S16 compares the non-resonant EELS at 1 eV incident energy computed with ωB97X-D and MP2 normal modes. We observe that the intensity of the first and second peaks is lower at the MP2 level than at the DFT level, which improves the agreement with the experimental spectra; however, the relative intensity pattern at the MP2 level is almost the same as that at the DFT level.

The energy loss ΔE equals

$$\Delta E = E_0 - E_{n'} = \sum_i m_i \omega_i, \tag{7}$$

where ω is the frequency of the normal mode and n is the number of quanta involved in each normal mode (n can only be 0 or 1—i.e., only one normal mode can be excited at a time). For each value of the incident energy, we computed the ICS for different energy losses using Eq. (4). As per Eq. (4), only the IR active modes were taken into account for the calculation of ICS. To account for anharmonicities, we scaled the computed frequencies by a factor of 0.95. The comparison between the scaled and unscaled calculations is shown in Fig. S17 in the supplementary material for the incident energy of 1 eV. We applied Gaussian broadening for the computed EELS (with FWHM = 0.01 eV).

We also analyzed the non-resonant EELS for selected energy losses corresponding to the six major peaks (59, 89, 133, 174, 388, and 437 meV). In these calculations, EELS were computed by summing over the normal modes with energies within 0.05 eV of a given energy loss. As discussed below, the peaks at 59 and 437 meV are due to a single normal mode each (NH out of plane bend and NH stretch, respectively), whereas the peaks at 89, 133, 174, and 388 meV comprise several normal modes. Four normal modes (at 385, 387, 389, and 390 meV) associated with C–H stretch were included in the 388 meV calculation. Six normal modes between 139 and 187 meV associated with C–H in-plane bend and ring deformation were included in the calculation of the 174 meV energy loss. Several normal modes due to ring deformation around 133 meV were included in the 133 meV peak. Four normal modes with frequencies between 75 and 106 meV, corresponding to C–H out-of-plane bends, were included in the 89 meV peak.

B. Calculations of EELS via resonances

To compute contributions to EELS via resonances, we used the ezFCF software[50,57] and the three models summarized in Fig. 2. The calculations of FCF require optimized geometries and frequencies for the initial and final states, and the quality of the computed spectra depends on both the absolute quality of the computed normal modes and the relative accuracy of the two calculations.[50] We experimented with several approaches and reported the results that show the best agreement with the experiment, i.e., DFT geometries and frequencies for the $^2B_2$ and $^2A_2$ resonances, and CCSD/EOM-CCSD geometries and frequencies for the $^2A_1$ resonance. The computed FCFs were convoluted with Gaussians (FWHM = 0.01 eV). The respective displacements and frequencies are given in the supplementary material.

EELS at 1 eV was computed using model 1 (direct detachment from the zero vibrational level of the resonance) and model 2 (with the excess energy of 0.45 eV distributed either thermally or equally). In these calculations, we used the geometry and frequencies of the $^2A_1$ state computed with CAP-EA-EOM-CCSD/aug-cc-pVDZ+2s2p and the geometry and frequencies of the neutral state computed with CCSD/aug-cc-pVDZ. In the FCF calculations, we took the resonance state as the initial state and neutral as the final state.

EELS at 2.5 eV with model 1 were computed using ωB97X-D/6-311++G** optimized geometries and frequencies for the neutral molecule and the $^2B_2$ state of the anion. In the FCF calculations, we took the resonance state as the initial state and neutral as the final state. All the normal modes were taken into consideration. The simulation was performed at 300 K.

EELS at 3.5 eV was first computed using model 1 (Fig. 2) with the same protocol as above (with ωB97X-D/6-311++G** structures and frequencies) and using the $^2A_2$ state as the initial state. Given that the lifetime of the $^2A_2$ resonance is very short, we also considered a process in which the initially populated $^2A_2$ state decays via a non-adiabatic transition to the $^2B_2$ state, which then ejects an electron, forming a vibrationally excited neutral state (models 2 and 3 in Fig. 2). In these calculations, we computed FCFs using optimized geometry and frequencies of the $^2B_2$ state as the initial state and then computed the spectrum either using Boltzmann populations corresponding to the excess energy of 0.43 eV or assuming a non-thermal population (i.e., an equal population of all vibrational levels accessible at the given excess energy).

All electronic structure calculations were carried out using the Q-Chem package.[58,59] The FCFs were computed using ezFCF.[50,57]

IV. EXPERIMENTAL DETAILS

Electron scattering experiments were performed on the electrostatic spectrometer.[60,61] The electrons were emitted from a heated iridium filament and energy-selected by a double-hemispherical electron monochromator. The electrons scattered on the effusive beam of the pure pyrrole vapor were analyzed with a double-hemispherical electron analyzer, which can be rotated in order to probe various scattering angles. The present data were recorded at a fixed scattering angle of 135°. We have chosen this angle because in electron scattering, the direct excitation processes related to direct-dipole excitation have cross sections peaking at small scattering angles.[31,62] The energy of the incident beam was calibrated using the 2^2S resonance in helium at 19.365 eV. The electron-energy resolution was 18 meV, as determined from the width of the elastic peak.

The pyrrole sample was purchased from Sigma–Aldrich and had a stated purity of 98%. In order to prevent condensation of the vapor, the sample container, gas inlet line, and effusive nozzle were kept at the temperature of 65 °C.

V. RESULTS AND DISCUSSION

A. Resonances in pyrrole: Theory

Figure 3 shows electronic states of pyrrole at its equilibrium geometry (Tables S3 to S12 in the supplementary material summarize the results obtained with various basis sets, Voronoi CAP, and CBF; the η-trajectories are shown in Figs. S1–S13).

The CAP-EOM-EA-CCSD calculations reveal four resonances. No other features suggestive of resonances were seen up to 8 eV; however, we cannot rule out the existence of electronic Feshbach resonances (i.e., of the 2-particle-1-hole type), whose energies would be overestimated by EOM-EA-CCSD calculations.[63,64]

The respective Dyson orbitals show the character of the resonances. In agreement with previous studies, we observe two π^* resonances—at 2.92 eV ($^2B_2$) and 3.53 eV ($^2A_2$), respectively. The upper resonance is quite broad (Γ = 0.92 eV, which corresponds to the lifetime of 0.72 fs). In addition, CAP-EOM-EA-CCSD yields two resonances at a lower energy of a σ-type: $^2A_1$ at 0.46 eV and $^2B_1$ at 1.10 eV. The lowest one ($^2A_1$) is especially interesting, as it shows electronic density localized around the N–H bond and is, therefore, expected to lead to DEA. The $^2B_1$ resonance resembles a quadrupole-bound state[65,66]—an analog of dipole-stabilized resonances[67]—in which the electron density of the attached electron is localized outside the molecular core. Pyrrole has a large quadrupole moment with large diagonal terms (Q_{xx} = −27.8, Q_{yy} = −34.82, and Q_{zz} = −24.67 debye-Å at the CCSD/aug-cc-pVDZ level). These values are larger than the quadrupole moment of the tetracyanobenzene anion, which was shown to support a quadrupole-bound anionic state.[66] Thus, we posit that the $^2B_1$ state may be a quadrupole-supported resonance.

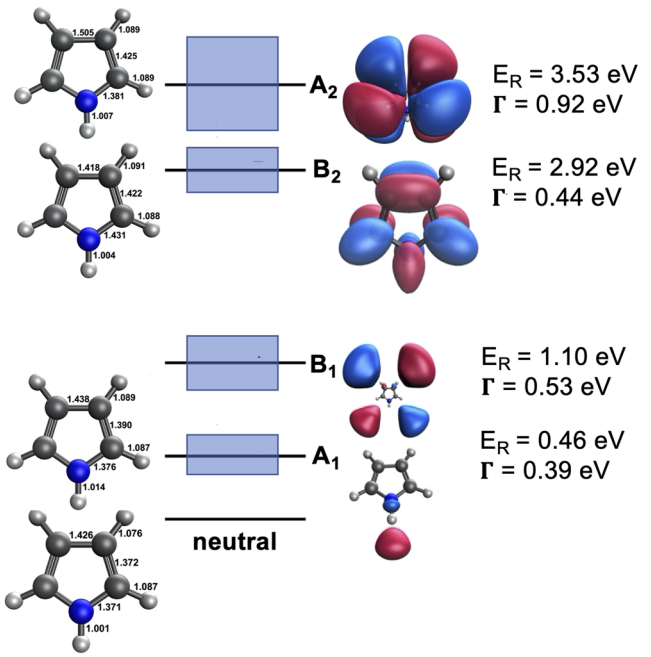

FIG. 3. Resonances in pyrrole. Energies and widths: zeroth-order CAP-EOM-EA-CCSD/aug-cc-pVDZ+4*s*3*p* with box-CAP; Dyson orbitals (real part): CAP-EOM-EA-CCSD/aug-cc-pVDZ+4*s*3*p*. Geometries optimized with CAP-EOM-EA-CCSD/aug-cc-pVDZ+4*s*3*p* (resonances) and CCSD/aug-cc-pVTZ (ground state of neutral pyrrole).

The optimized geometries (Fig. 3) are consistent with the shape of the Dyson orbitals. In the $^2A_1$ state (σ^* resonance), the Dyson orbital is localized around the N–H bond, and the respective optimized geometry shows a 0.013 Å increase in the N–H bond length. Furthermore, the C=C and C–C distances increase by 0.018 and 0.013 Å, respectively. The C–H bonds also show a slight increase (0.012 Å). In the $^2B_2$ state (the lower π^* resonance), the Dyson orbital has an anti-bonding character with respect to the C=C and C–N bonds, and we observe an increase of 0.05 and 0.06 Å for these bonds. In contrast, the Dyson orbital shows bonding character with respect to the C–C bond, and we indeed observe a slight decrease of 0.007 Å. The change in the N–H bond length is negligible (0.003 Å). The Dyson orbital for the $^2A_2$ resonance (higher π^*) has more nodes, which results in a structure in which all bonds are elongated relative to the neutral.

Tables S3–S11 in the supplementary material show the results of CAP calculations using two different CAPs (box and Voronoi) and various basis sets. In the box-CAP calculations with the double-zeta bases, the results are nearly converged at the 4*s*3*p* level (variations less than 0.04 eV for energies and 0.02 for the widths). The difference between the aug-cc-pVDZ+4*s*3*p* and aug-cc-pVTZ+3*s*3*p* calculations is relatively small for the three lowest resonances (0.2/0.3 eV), but for the $^2A_2$ state the differences are larger—0.4/0.6 eV for energy/width.

The Voronoi calculations with a CAP onset of 4.13 Å (which matches roughly the size of the box CAP in the molecular plane) could not locate the upper π^* resonance plane; however, this state was found in the calculations with a smaller onset of 3.00 Å (which matches better the box CAP onset perpendicular to the molecular plane).

The largest differences between the box-CAP and Voronoi-CAP in the smallest basis (aug-cc-pVDZ+2*s*2*p*) are 0.18/0.13 eV, but they become smaller as the basis set increases. In the aug-cc-pVDZ+4*s*3*p* basis, the largest differences are 0.2/0.1 eV for the three lowest resonances and 0.2/0.2 for the $^2A_2$ state.

The CBF calculations (Table S12 in the supplementary material) confirmed the results of the CAP calculations for all four resonances. The calculations with a smaller basis (2*s*2*p*) failed to reproduce the $^2B_1$ resonance, but using a larger basis (4*s*2*p*) yielded a nice trajectory showing a clear stabilization point. For all four resonances, the agreement between CAP-EOM-CCSD and CBF-EOM-CCSD is also improved in the larger basis, with the maximum difference being observed for the $^2A_2$ state (0.13 eV for energy and 0.56 eV for width, as compared to the box-CAP/aug-cc-pVDZ+4*s*3*p* calculation). We note that in our studies of the cyanopolyyne anion,[53] CAP calculations sometimes produced low-lying resonances that were not confirmed by CBF calculations. Hence, the agreement between the CBF and CAP calculations is reassuring that the resonances observed in both the CAP and CBF calculations are indeed real.

Therefore, the four resonances shown in Fig. 3 are confirmed by three different approaches: CBF, box-CAP, and Voronoi-CAP.

The appearance of the σ^*-like resonance below the π^* resonances may appear surprising, as anti-bonding σ^* orbitals are located above π^* orbitals, and only when the respective bond is stretched, their energies drop—this trend was observed in photochemical[32] and DEA[4–7] processes in aromatic molecules (and more recently[43] in C_2H^-). The analysis of the Dyson orbital and the energy along the N–H bond stretch provides an explanation for this result.

Figure 4 shows the PES scan for the lowest resonance along the N–H stretching coordinate as well as the changes in the Dyson orbital. At equilibrium geometry, the shape of the Dyson orbital resembles that of a dipole-bound state (DBS), similar to the dipole-stabilized resonances observed earlier in molecules with large dipole moments.[67] Indeed, pyrrole has a relatively large dipole moment—1.86 debye at CCSD/aug-cc-pVDZ or 1.74 debye experimental.[68] The configuration interaction between the σ^* and DBS-like configurations stabilizes this resonance. As the N–H bond is stretched, the Dyson orbital changes, revealing the increased contributions of the σ^* configuration. Accordingly, the PES of this state along the N–H bond breaking is shallow, showing lower dissociation energy than the neutral state, thus suggesting effective DEA of the N–H bond. We note that at a moderately stretched N–H bond (~1.4 Å), this resonance becomes electronically bound. Hence, one may expect spectral signatures of this state similar to vibrational Feshbach resonances; we discuss this issue below. We note that Γ drops to zero at a slightly longer bond length than the crossing point of the real potential energy curves (Γ at MECP is 0.19 eV), indicating the remaining perturbation due to the CAP;[69] similar deviations from the ideal behavior were noted by Benda and Jagau.[55]

To estimate adiabatic positions of resonances, we computed their energies at the respective optimized geometries of the $^2A_1$, $^2B_2$, and $^2A_2$ resonances; the shape of the Dyson orbital for the $^2B_1$ resonance is such that no geometry change is expected for this state, so that adiabatic and vertical attachment energies are the same. The energetic relaxation for the three resonances is moderate, e.g., 0.06 eV ($^2A_1$), 0.29 eV ($^2B_2$), and 0.26 eV ($^2A_2$). A larger relaxation in the two π-resonances is consistent with the shapes of the respective Dyson orbitals. The computed zero-point energies (see the supplementary material) are very similar (within 1 kcal/mol) in the neutral and resonances; therefore, the adiabatic ΔE_{ee} are good approximations to the adiabatic ΔE_{00} values (shown in Table S16).

Although zero-point vibrational corrections have a negligible effect on the ΔE_{00} values, they are very important for the lifetime of the σ^* resonance. As shown in Fig. 4, the σ^* resonance becomes stabilized (i.e., its energy drops below the neutral) and moderately stretched N–H bond, e.g., around 1.4 Å (if other degrees of freedom are frozen). We optimized the location of the MECP between the resonance and the neutral and found that the N–H bond length is indeed the key structural parameter leading to resonance stabilization. When other degrees of freedom are allowed to relax, the resonance is stabilized at r_{NH} = 1.34 Å (the inset in the right panel of Fig. 4 shows the MECP structure). Energetically, the MECP is located 0.8 eV above the minimum of the resonance. That means that the lowest vibrational level for the N–H stretch is only 0.32 eV below the MECP, and already the second vibrational level is above the MECP. Hence, one quanta of vibrational excitation in this mode should result in a significant increase in the lifetime of this state. This provides an explanation for the low-energy sharp feature observed in the ET experiments,[35] alternative to that invoking a virtual state. The present experiment, discussed below in Sec. V B, shows that a similar sharp feature appears in the excitation of the N–H stretch mode [Fig. 9(f)], whereas broader features at ~0.5 eV are visible for the C–H bend and ring deformations (0.174 eV energy loss) and the C–H stretch (0.388 eV). We note that the physical reasons for the existence of the low-lying σ^* resonance and its stabilization by the N–H stretch—the interplay between dipole-stabilized and σ^*_{NH}

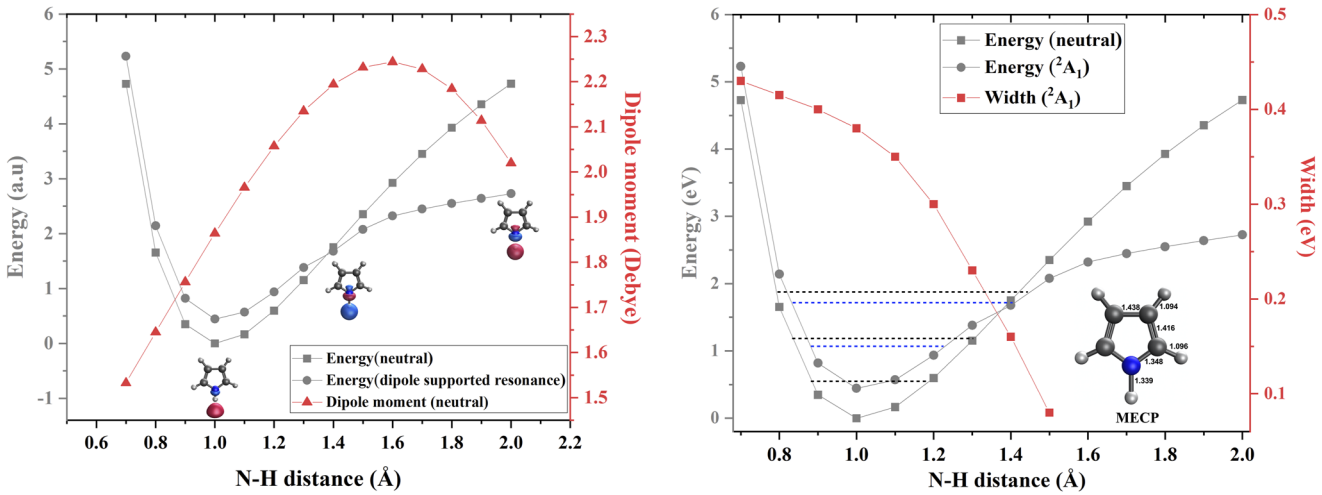

FIG. 4. Potential energy curves for the neutral and $^2A_1$ resonance states of pyrrole. The left panel shows the dipole moment (CCSD/aug-cc-pVDZ) of the neutral molecule along the N–H stretch and the real part of the Dyson orbital. Dashed lines in the right panel show the vibrational levels for the N–H stretch for the neutral (black) and for the resonance (blue), and the inset shows the MECP structure.

configurations—were identified already in Ref. 35; however, the level of electronic structure theory used in this work was not sufficient to capture this resonance, and the explanation invoked a virtual state. In contrast, our calculations provide a consistent explanation of the experimental features in terms of the low-lying σ^* resonance state. We note that scattering close to a threshold is strongly influenced by non-local effects due to the possibility of a re-attachment of the (slow) outgoing electron. In the nonlocal treatment, the effects of resonances, virtual states, and bound states have to be included, and it is not easy to distinguish between them.[70,71]

Figure 5 shows PES scans for the four computed resonances along the N–H bond length (with all other degrees of freedom being fixed). As one can see, only the lowest resonance asymptotically correlates with the lowest DEA threshold at which the DEA signal has been experimentally observed.[72,73]

B. EELS: Theory vs Experiment

Figure 6(a) shows the experimental EELS. It is constructed from individual one-dimensional energy loss spectra recorded at incident electron energies with 10 meV increments. Such a color-coded map can reveal the complex dynamics of nuclear motion induced by electron scattering.[23,74,75] The details of this dynamics in pyrrole (and of its influence on the dissociative attachment) are presented elsewhere.[76] The two-dimensional spectrum features several prominent peaks persisting in the entire energy range of the incident electrons. It also shows an increase in intensity around 2.5 and 3.5 eV, suggestive of resonances. The presence of resonances becomes more visible by looking at the intensities of the individual vibrational excitations as a function of incident energies (scans of the EELS along vertical lines). Scans along horizontal lines show EELS for a given incident energy.

Figure 6(b) shows the theoretical EELS map computed using non-resonant treatment, Eq. (4). In this regime, the positions of the dominant EELS features correspond to the IR peaks. The computed IR spectrum of pyrrole is shown in Fig. 7; the summary of frequency calculations is given in Fig. S14 in the supplementary material. The IR spectrum shows six major peaks at 0.053, 0.085, 0.125, 0.178, 0.388, and 0.443 eV. The low-energy peaks correspond to ring bending vibrations: the peaks at 53 and 85 meV correspond to a single mode—N–H out-of-plane bend (mode 0 of symmetry b_2) and C–H out-of-plane bend (mode 4 of symmetry b_2), respectively, whereas the peaks at 125, 178, and 388 meV comprise several vibrations. The peak at 125 meV is due to modes 8 and 9 of a_1 symmetry and modes 10, 11, and 12 of b_1 symmetry, which correspond to ring deformation, and the peak at 178 meV is due to modes 13 (a_1), 14 (b_1), 15 (a_1), 16 (b_1), 17 (a_1), and 18 (b_1), corresponding to the ring deformation and C–H bending vibrations. The peak at 443 meV corresponds to the N–H stretching vibration (mode 21 of a_1 symmetry). The low-intensity peak at 388 meV comprises several C–H vibrations: modes 19 (a_1), 20 (a_1), 21 (a_1), and 22 (a_1). The intensity ratio of these peaks in the EELS differs from the IR intensities and depends on the incident energy. In particular, the intensity of all peaks decreases with the increasing incident energy, e.g., the intensity of the lowest-energy peak drops by a factor of three as the incident energy increases from 0.75 to 3.5 eV. The intensity of higher-energy loss peaks decreases slower than that of the low-energy loss peaks, such that the relative

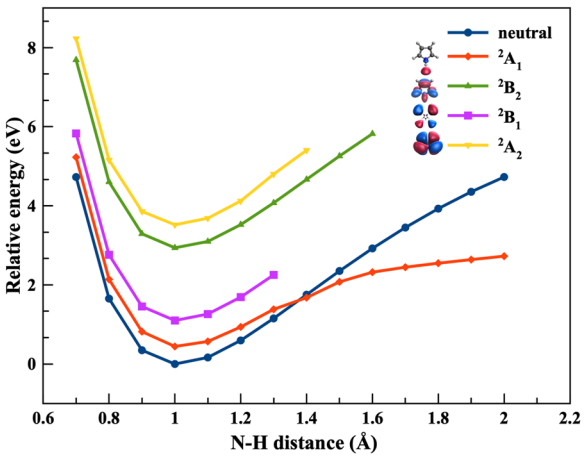

FIG. 5. Potential energy curves for the neutral and resonance states of pyrrole. Curves for resonances were computed with CAP-EOM-EA-CCSD/aug-cc-pVDZ+4*s*3*p*, and the neutral curve was computed with CCSD/aug-cc-pVDZ.

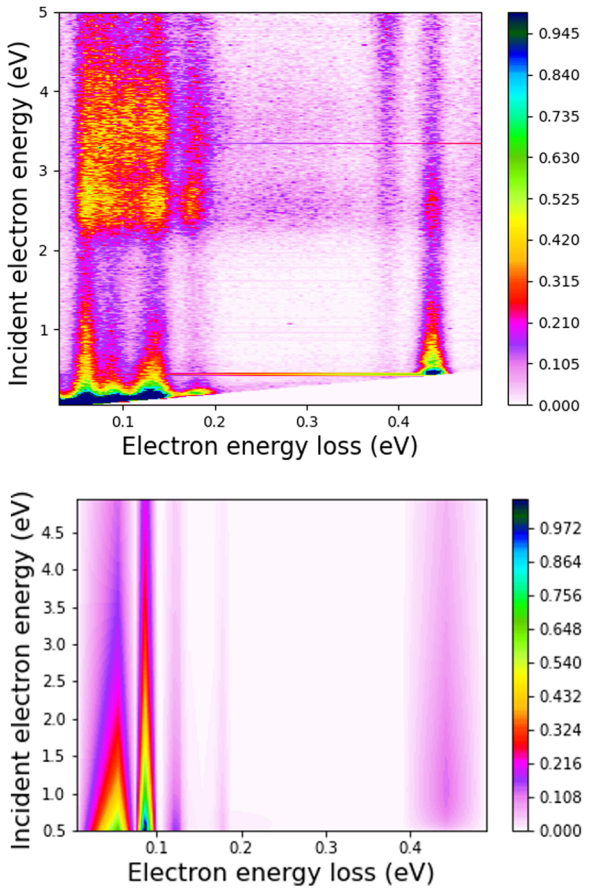

FIG. 6. Two-dimensional EELS maps. Top: Experimental EELS. Bottom: Theoretical EELS for non-resonant energy loss. The elastic peak is not shown.

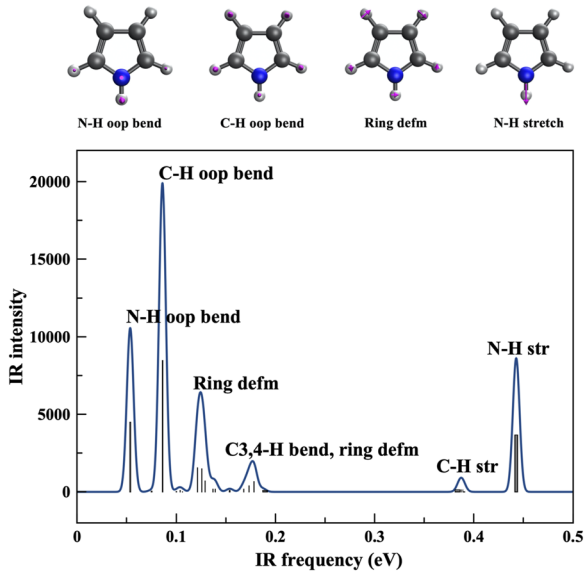

FIG. 7. Simulated IR spectra with scaled frequencies. Selected normal modes are shown on top.

ratio of the high-energy peaks increases at higher incident energy. These trends are clearly seen in the horizontal cuts (energy loss for selected incident energies shown in Fig. S18 in the supplementary material).

Figure 8 shows the theoretical and experimental EELS for 1 eV incident energy. As one can see, the positions of the main peaks are well reproduced by the calculations; however, the relative intensities are somewhat off. In particular, the intensity of the second peak (at 89 meV energy loss) is overestimated by the calculation, and the intensity of the two high-energy peaks (388 and 437 meV) is underestimated. There are several possible reasons for this discrepancy—limitations of the theoretical model

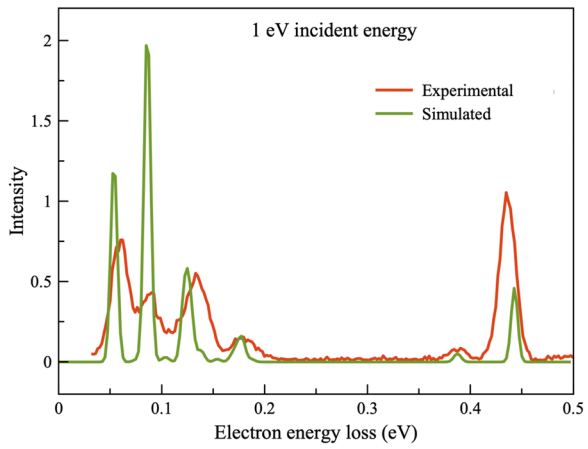

FIG. 8. Experimental (red) EELS and simulated (green) threshold excitation spectra at 1.0 eV incident energies.

for ICS [i.e., Eq. (4)], the experimental setup[62] (e.g., in the experiment, the scattered electrons are collected at a fixed angle and not integrated over all angles), harmonic approximation, or inaccuracies in the quantum-chemistry method used to compute frequencies. In addition, the disagreement could be (at least in part) due to the contribution from scattering via the resonances—according to the calculations, even at 1 eV of incident energy, the $^2A_1$ resonance is accessible.

Figure 9 shows the experimental and computed excitation curves for the six dominant peaks (vertical cuts, see Fig. 6). The initial decay of the intensity is reproduced relatively well for the two lowest peaks (59 and 89 meV), but not for the higher peaks.

Figure 9 shows clear signatures of the two π resonances at about 2.5 and 3.5 eV. We note that the exact positions of the maxima on the experimental energy loss curves are not the same, showing variations up to 0.16 eV (see Table S2 in the supplementary material), because resonances contribute differently to different vibrational modes. Overall, it is not obvious how the experimental peak maxima should be compared with theory. In analogy with the spectroscopy of bound states,[50] one may expect that the highest intensity corresponds to the adiabatic energy difference. In the recent theoretical study[77] of acrylonitrile and methacrylonitrile, Jagau and co-workers reported that the EELS peak maxima agree better with the computed adiabatic energies of resonances than with the vertical energy gaps. They reported discrepancies between the theory (CAP-EOM-CCSD) and experiment of roughly 0.3 eV, which is consistent with the error bars of this level of correlation treatment.

Our calculations place the two π resonances at 2.92 and 3.53 eV vertically and 2.63 and 3.27 eV adiabatically, which agrees reasonably well with the experimental features within ~0.3 eV, as in the case of acrylonitrile and methacrylonitrile.[77]

The resonance contributions affect different energy loss peaks to a various extent, which is related to the structural changes induced by electron attachment. For example, electron attachment to anti-bonding π^* orbitals is expected to affect ring deformation modes and out-of-plane vibrations, which are clearly seen in panels (a)–(d). In contrast, the N–H stretch is affected only weekly, which leads to relatively small resonance peaks for 437 meV energy loss.

According to the calculations, there is a low-lying resonance at 0.5 eV. As per Fig. 3, the σ^* resonance is expected to affect the N–H stretch. The resonance is broad, such that one may expect its contributions to be smeared in the low-energy range, thus affecting the trends in the individual EELS intensities. Importantly, the resonance becomes stabilized upon vibrational excitation, and already one quanta in the NH stretch brings the energy above the MECP with the neutral. Thus, one can expect to see a sharp increase in the ICS at about 0.90 eV (0.46 + 0.44 eV, see Fig. 4). Panel (f) of Fig. 9 indeed shows a sharp feature at 0.84 eV.

The CAP calculations also yield a resonance state at 1.1 eV ($^2B_1$). This state is confirmed by the CBF calculations when using a sufficiently large basis set. As far as the signatures of this putative $^2B_1$ resonance are concerned, one cannot expect to see evidence of direct scattering via this state because its structure is nearly the same as the structure of the neutral, so that the respective FCFs are diagonal and there are no contributions to the inelastic ICS. However, this state may, in principle, show up via an indirect process (model 3 in Fig. 2), leading to the enhancement of the features due to the $^1A_1$

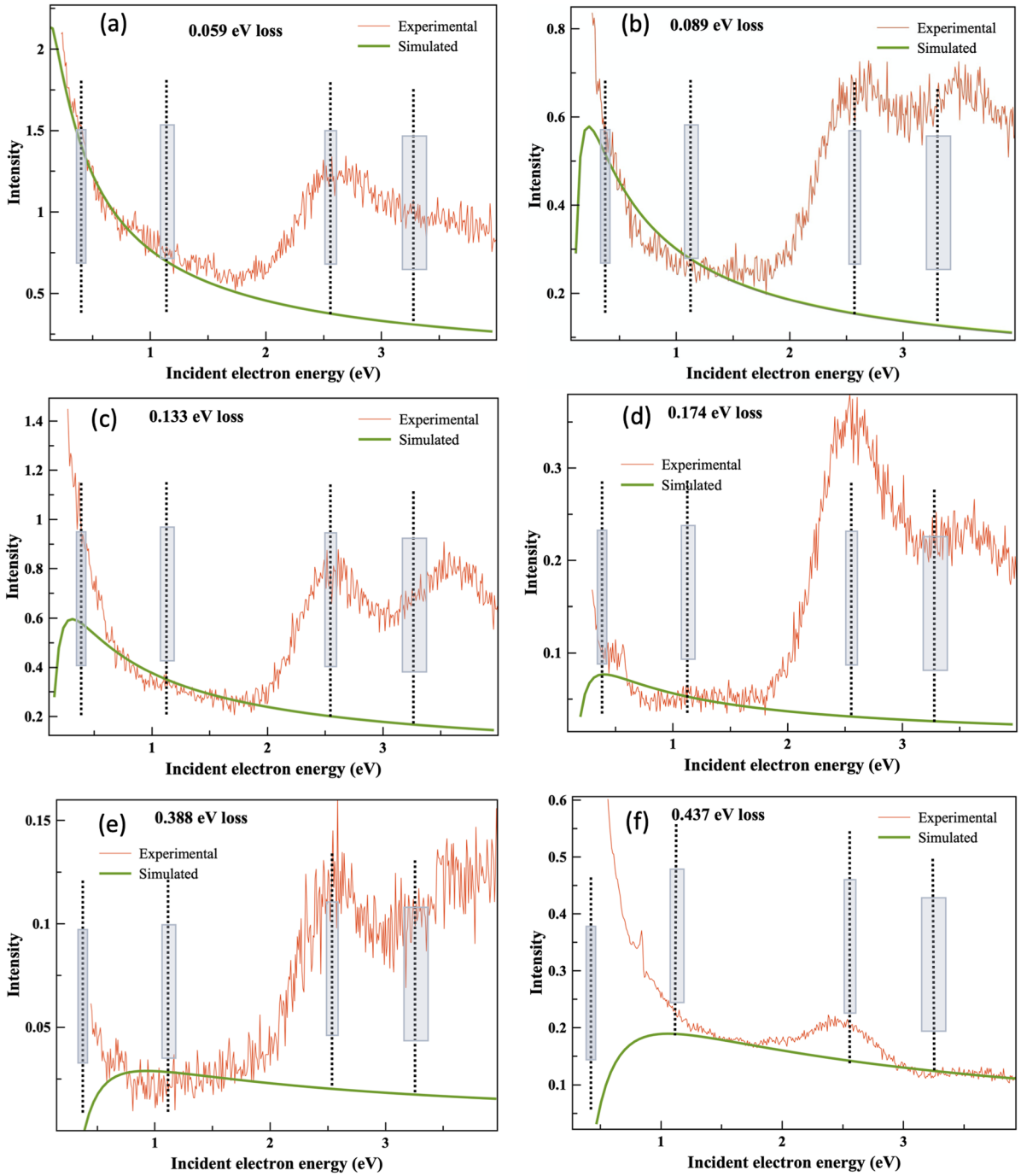

FIG. 9. Experimental and simulated excitation curves at individual energy losses. The positions (E_{00}) and widths of the computed resonances are shown in gray.

resonance. In sum, current EELS results neither prove nor disprove its existence.

As Fig. 9 shows, the width of the threshold peaks (e.g., how fast they decay as the incident energy increases) is reproduced by the calculations only for the two low peaks [panels (a) and (b)], whereas for the higher energy losses [panels (c)–(f)], the experimental peaks are much narrower. As mentioned above, there are a few effects that could contribute to this discrepancy. The most

significant one[62] is that Eq. (4) is valid for the integral cross section (over all scattering angles), whereas the experimental data correspond to the differential cross section at the scattering angle of 135°; hence, a possible angular dependence of the threshold behavior could be responsible for the discrepancy, especially because the dominant contribution to the ICS is the forward-peaked direct dipolar contribution. Another possible explanation is that the threshold behavior is affected by the low-lying σ^* resonance, which, according to calculations, appears at 0.46 eV. The calculations of the vibrational excitations due to the σ^* resonance (discussed in Sec. I below) suggest that scattering through this resonance would not affect the two lowest bending modes but should contribute to the higher energy losses. We note that irregularities in threshold behavior (e.g., sharp threshold peaks) were observed in several molecules, e.g., CO_2,[78,79] NCCN,[80] and $Fe(CO)_5$,[81] and explained by invoking the existence of a virtual state.[70] As already explained in the discussion of the sharp feature in the NH stretch excitation (Sec. V A), the presently identified σ^* resonance can lead to similar effects, manifested here in the shape of the threshold peaks.

1. EELS due to scattering via resonances

Figure 10 shows EELS due to scattering via the resonances computed using model 1 (see Fig. 2). At the incident energy of 1 eV [panel (a)], the resonant scattering contributes to energy loss peaks 3–6 (133, 174, 388, and 437 meV). Because of the low intensity of the peaks at 174 eV and 388 meV, the resonance contributions are more prominent—indeed, individual energy loss scans [panels (d) and (e) in Fig. 9] show broad features around 0.5 eV. The energy loss at 437 meV [N–H vibration, panel (f)] shows a sharp feature attributed to the vibrational Feshbach resonance (one quanta in the N–H stretch).

At the incident energy of 2.5 eV, scattering via the $^2B_2$ resonance leads to the appearance of new peaks in a higher energy range that are not present in the computed non-resonant spectra but are clearly seen in the experimental EELS. At the incident energy of 3.5 eV, calculations of the scattering via the $^2A_2$ resonance show contributions to the low energy loss peaks.

To assess the effect of the excess energy, we computed EELS at 1 eV incident energy using model 2. Figure S22 compares three different calculations. The effect of excess vibrational energy appears in low-energy energy loss peaks. We see a slight improvement with model 2.

Figure S23 shows the calculation of EELS at 3.5 eV incident energy using 3 different models. We see that model 3 gives better agreement; in particular, it explains a peak of around 0.2 eV of energy loss, which is not seen in the non-resonant regime. Moreover, model 3 explains new features at higher energy loss.

Figure 11 shows experimental and computed EELS at the three incident frequencies (1, 2.5, and 3.5 eV) computed by combining non-resonant and resonant contributions. For EELS at 1, 2.5, and 3.5 eV, the resonant contribution was computed with model 2, model 1, and model 3, respectively. The non-resonant EELS was simulated at the respective incident energies and added to the resonant contributions. The combined spectra that include the contributions from both the resonant and non-resonant regimes reproduce all major features in the experimental spectra at the three incident energies. We consider this agreement to be reasonably good, given the already-mentioned multiple factors, both from the experimental and theoretical sides, that may contribute to the discrepancies.

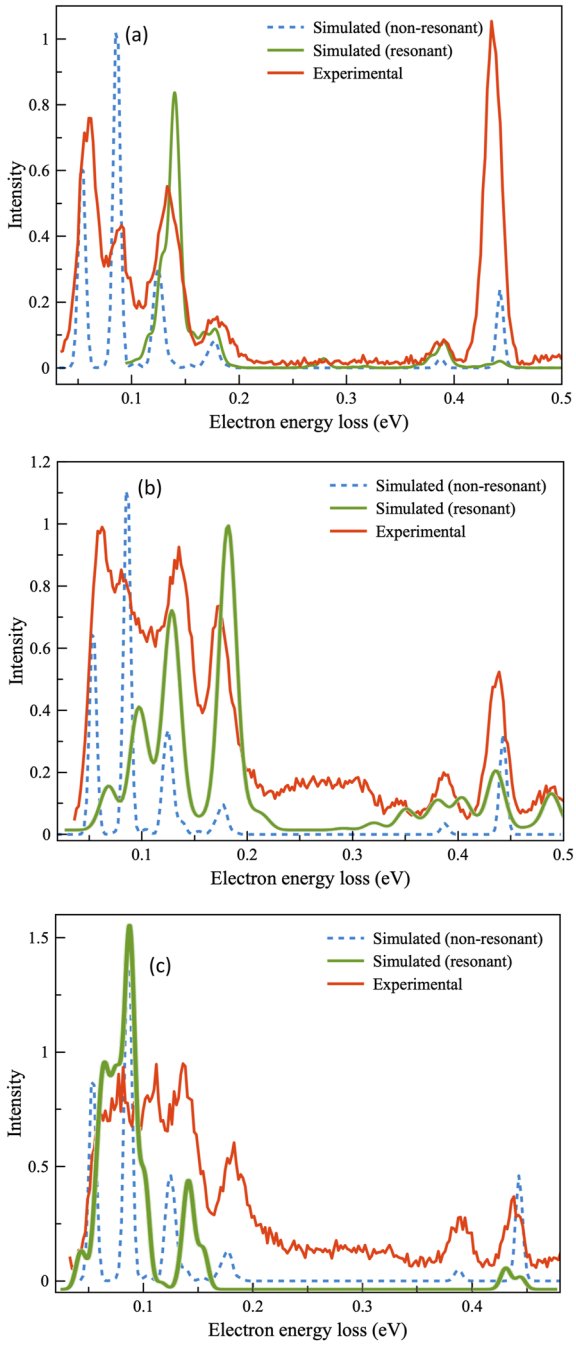

FIG. 10. EELS at the three selected incident energies via the $^2A_1$ [1 eV, panel (a)], $^2B_2$ [2.5 eV, panel (b)], and $^2A_2$ [3.5 eV, panel (c)] resonances computed using model I. The dashed blue line shows non-resonant vibrational excitations.

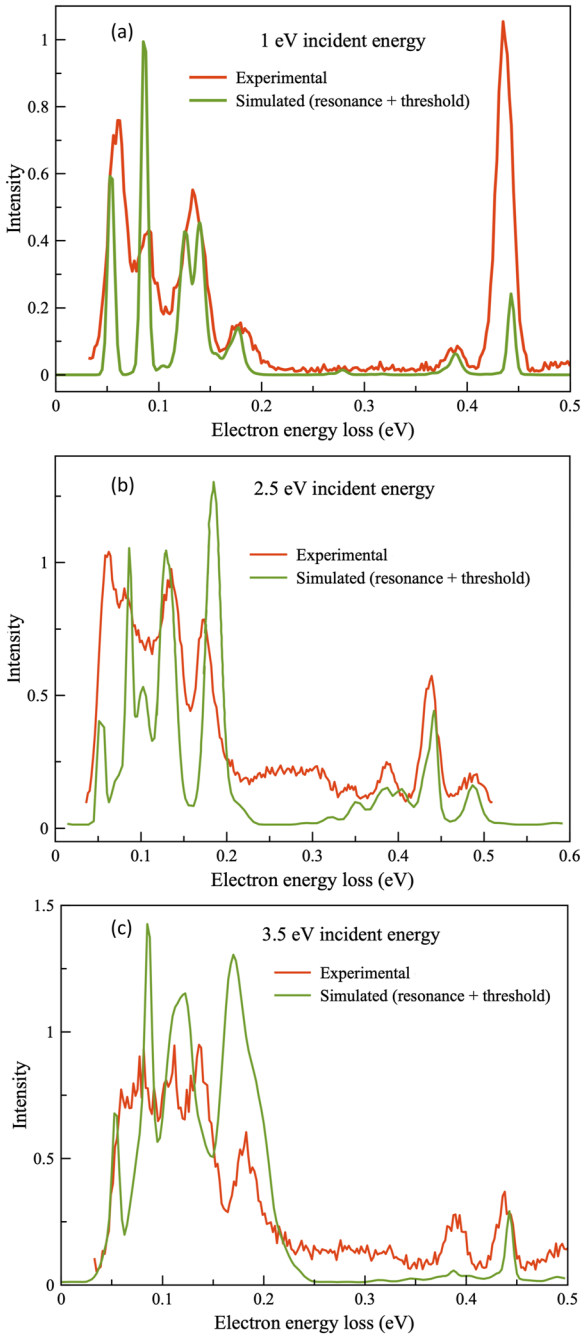

FIG. 11. EELS at the three incident energies, including non-resonant and resonant contributions (see text).

VI. CONCLUSIONS

We report a combined theoretical and experimental study of electron scattering from pyrrole. Two-dimensional EELS provide detailed information about molecular vibrational energy levels and resonances. The patterns in energy loss due to resonances report on the shapes of the underlying PES. Electronic structure calculations allowed us to assign all major features and trends in the EELS. We observed clear spectroscopic signatures of two π^* resonances as well as a low-lying σ^* resonance. The broad features in the EELS due to the two π^* resonances appear at about 2.5 and 3.5 eV. Our calculations place these two resonances at 2.92 and 3.53 eV vertically and 2.63 and 3.27 eV adiabatically, which agrees reasonably well with the experimental features, within the typical error bars of EOM-EA-CCSD. The calculations of vibrational excitations due to the scattering via these resonances explain the changes in vibrational patterns in the EELS compared to the non-resonant (threshold) excitations. The calculations also predict a low-lying resonance at 0.46 eV, which has a mixed character—of a DBS and σ^* type. The configuration interaction between these two configurations is responsible for its low energy. The corresponding PES features low dissociation energy for the N–H bond and, therefore, can lead to DEA. This resonance becomes stabilized at one quanta of the NH excitation, giving rise to the sharp feature at ~0.9 eV in the corresponding energy loss spectrum. The calculations of the vibrational excitation due to scattering via this resonance suggest that it can affect the threshold behavior of higher energy loss peaks. Specifically, less prominent, broader features around 0.5 eV at 0.147 and 0.388 eV energy losses are likely to be due to this resonance.

Non-Hermitian extensions of modern quantum chemistry methods, such as complex-valued EOM-CC, are capable of describing electron correlations of resonance states and, therefore, can yield a quantitative description of resonances, their Dyson orbitals, and their PES. These tools allowed us to explain the observed features in the experimental EELS by using the concepts of non-Hermitian quantum chemistry,[12–14,27] such as complex PES[54,55,69] and Dyson orbitals.[82,83] The physical significance of these molecular quantum chemistry concepts is illustrated by calculations of FCFs, which can be directly compared with the observed features in the EELS at resonant energies.

Our study also highlights persistent challenges in understanding electron–molecule interactions. The experimental studies of resonances are far from being trivial and produce noisier and less well-resolved spectra compared to spectroscopies probing bound states. The theoretical treatment of spectroscopic signatures of resonances is also more difficult compared to bound states. Treating resonant and non-resonant contributions to EELS on the same footing is not yet possible. The comparison between the theory and experiment involves a number of assumptions and approximations. We hope that our work will motivate further experimental and theoretical developments aiming to achieve the same level of precision and accuracy as in the case of spectroscopic studies of bound states.

SUPPLEMENTARY MATERIAL

The supplementary material contains the data of previous studies of pyrrole resonances, experimental EELS peak maxima, additional results of calculations of resonances using CAP and CBF methods, details about the optimization of the resonance states, calculations of frequencies, normal mode analysis of the neutral molecule and the resonant states, as well as additional information about the calculation of EELS via resonances and relevant Cartesian coordinates.

ACKNOWLEDGMENTS

A.I.K. acknowledges financial support from the U.S. National Science Foundation through the CHE-2154482 Grant. J.F. acknowledges support from Czech Science Foundation Project No. 21-26601X and from Ministry of Education, Youth and Sports of the Czech Republic Project No. LTAUSA19031.

AUTHOR DECLARATIONS

Conflict of Interest

A.I.K. is the president and part-owner of Q-Chem.

Author Contributions

Madhubani Mukherjee: Data curation (lead); Formal analysis (lead); Investigation (equal); Software (equal); Visualization (lead); Writing – original draft (equal). **T. P. Ragesh Kumar**: Investigation (equal). **Miloš Ranković**: Investigation (equal). **Pamir Nag**: Investigation (equal). **Juraj Fedor**: Conceptualization (equal); Formal analysis (equal); Funding acquisition (equal); Methodology (equal); Project administration (equal); Resources (equal); Supervision (equal); Validation (equal); Writing – original draft (equal); Writing – review & editing (equal). **Anna I. Krylov**: Conceptualization (equal); Formal analysis (equal); Funding acquisition (equal); Methodology (equal); Project administration (equal); Resources (equal); Software (equal); Supervision (equal); Validation (equal); Writing – original draft (equal); Writing – review & editing (equal).

DATA AVAILABILITY

The data that support the findings of this study are available within the article and its supplementary material.

REFERENCES

[1] I. I. Fabrikant, S. Eden, N. J. Mason, and J. Fedor, "Recent progress in dissociative electron attachment: From diatomics to biomolecules," Adv. At. Mol. Opt. Phys. **66**, 545 (2017).

[2] P. Christopher, H. Xin, A. Marimuthu, and S. Linic, "Singular characteristics and unique chemical bond activation mechanisms of photocatalytic reactions on plasmonic nanostructures," Nat. Mater. **11**, 1044 (2012).

[3] P. Rumbach and D. B. Go, "Chapter perspectives on plasmas in contact with liquids for chemical processing and materials synthesis," *Topics in Catalysis* (Springer, 2013), Vol. 56.

[4] J. Simons, "Molecular anions," J. Phys. Chem. A **112**, 6401 (2008).

[5] J. Simons, "Theoretical study of negative molecular ions," Annu. Rev. Phys. Chem. **62**, 107 (2011).

[6] J. Simons, "Detachment processes for molecular anions," in *Photoionization and Photodetachment*, Part II of Advanced Series in Physical Chemistry, edited by C. Y. Ng (World Scientific Publishing Co., Singapore, 2000), Vol. 10.

[7] J. M. Herbert, "The quantum chemistry of loosely-bound electrons," Rev. Comput. Chem. **28**, 391 (2015).

[8] B. Boudaïffa, P. Cloutier, D. Hunting, M. A. Huels, and L. Sanche, "Resonant formation of DNA strand breaks by low-energy (3 to 20 eV) electrons," Science **287**, 1658 (2000).

[9] J. Simons, "How do low-energy (0.1–2 eV) electrons cause DNA-strand breaks?," Acc. Chem. Res. **39**, 772 (2006).

[10] B. M. Penetrante, M. C. Hsiao, J. N. Bardsley, B. T. Merritt, G. E. Vogtlin, A. Kuthi, C. P. Burkhart, and J. R. Bayless, "Identification of mechanisms for decomposition of air pollutants by non-thermal plasma processing," Plasma Sources Sci. Technol. **6**, 251 (1997).

[11] T. Matsumoto, D. Wang, T. Namihira, and H. Akiyama, "Energy efficiency improvement of nitric oxide treatment using nanosecond pulsed discharge," IEEE Trans. Plasma Sci. **38**, 2639 (2010).

[12] W. P. Reinhardt, "Complex coordinates in the theory of atomic and molecular structure and dynamics," Annu. Rev. Phys. Chem. **33**, 223 (1982).

[13] N. Moiseyev, *Non-Hermitian Quantum Mechanics* (Cambridge University Press, 2011).

[14] S. Klaiman and I. Gilary, "On resonance: A first glance into the behavior of unstable states," Adv. Quantum Chem. **63**, 1 (2012).

[15] T.-C. Jagau, K. B. Bravaya, and A. I. Krylov, "Extending quantum chemistry of bound states to electronic resonances," Annu. Rev. Phys. Chem. **68**, 525 (2017).

[16] A. I. Krylov, "Equation-of-motion coupled-cluster methods for open-shell and electronically excited species: The hitchhiker's guide to Fock space," Annu. Rev. Phys. Chem. **59**, 433 (2008).

[17] K. Sneskov and O. Christiansen, "Excited state coupled cluster methods," WIREs: Comput. Mol. Sci. **2**, 566 (2012).

[18] R. J. Bartlett, "Coupled-cluster theory and its equation-of-motion extensions," WIREs: Comput. Mol. Sci. **2**, 126 (2012).

[19] M. Ehara and T. Sommerfeld, "CAP/SAC-CI method for calculating resonance states of metastable anions," Chem. Phys. Lett. **537**, 107 (2012).

[20] M. Ehara, R. Fukuda, and T. Sommerfeld, "Projected CAP/SAC-CI method with smooth Voronoi potential for calculating resonance states," J. Comput. Chem. **37**, 242 (2016).

[21] A. Dreuw and M. Wormit, "The algebraic diagrammatic construction scheme for the polarization propagator for the calculation of excited states," WIREs: Comput. Mol. Sci. **5**, 82 (2015).

[22] T.-C. Jagau, "Theory of electronic resonances: Fundamental aspects and recent advances," Chem. Commun. **58**, 5205 (2022).

[23] K. Regeta and M. Allan, "Autodetachment dynamics of acrylonitrile anion revealed by two-dimensional electron impact spectra," Phys. Rev. Lett. **110**, 203201 (2013).

[24] M. Allan, K. Regeta, J. D. Gorfinkiel, Z. Mašín, S. Grimme, and C. Bannwarth, "Recent research directions in fribourg: Nuclear dynamics in resonances revealed by 2-dimensional EEL spectra, electron collisions with ionic liquids and electronic excitation of pyrimidine," Eur. Phys. J. B **70**, 123 (2016).

[25] G. Jolicard and E. J. Austin, "Optical potential stabilisation method for predicting resonance levels," Chem. Phys. Lett. **121**, 106 (1985).

[26] U. V. Riss and H.-D. Meyer, "Calculation of resonance energies and widths using the complex absorbing potential method," J. Phys. B **26**, 4503 (1993).

[27] R. Santra and L. S. Cederbaum, "Non-Hermitian electronic theory and applications to clusters," Phys. Rep. **368**, 1 (2002).

[28] C. W. McCurdy and T. N. Rescigno, "Extension of the method of complex basis functions to molecular resonances," Phys. Rev. Lett. **41**, 1364 (1978).

[29] A. F. White, M. Head-Gordon, and C. W. McCurdy, "Complex basis functions revisited: Implementation with applications to carbon tetrafluoride and aromatic N-containing heterocycles within the static-exchange approximation," J. Chem. Phys. **142**, 054103 (2015).

[30] A. F. White, E. Epifanovsky, C. W. McCurdy, and M. Head-Gordon, "Second order Møller-Plesset and coupled cluster singles and doubles methods with complex basis functions for resonances in electron-molecule scattering," J. Chem. Phys. **146**, 234107 (2017).

[31] Y. Itikawa, "Electron-impact vibrational excitation of polyatomic molecules," Int. Rev. Phys. Chem. **16**, 155 (2010).

[32] M. N. R. Ashfold, G. A. King, D. Murdock, M. G. D. Nix, T. A. A. Oliver, and A. G. Sage, "π–σ^* excited states in molecular photochemistry," Phys. Chem. Chem. Phys. **12**, 1218 (2010).

[33] A. Modelli, P. D. Burrow, and V. Selmi, "Electron attachment to the aza-derivatives of furan, pyrrole, and thiophene," J. Phys. Chem. A **108**, 5721 (2004).

[34]E. M. De Oliveira, M. A. P. Lima, M. H. F. Bettega, S. D. A. Sanchez, R. F. Da Costa, M. T. d. N. Varella, and N. Varella, "Low-energy electron collisions with pyrrole," J. Chem. Phys. **132**, 204301 (2010).
[35]S. A. Pshenichnyuk, I. I. Fabrikant, A. Modelli, S. Ptasinska, and A. S. Komolov, "Resonance electron interaction with five-membered heterocyclic compounds: Vibrational Feshbach resonances and hydrogen-atom stripping," Phys. Rev. A **100**, 012708 (2019).
[36]O. May, J. Fedor, B. C. Ibănescu, and M. Allan, "Absolute cross sections for dissociative electron attachment to acetylene and diacetylene," Phys. Rev. A **77**, 040701 (2008).
[37]O. May, J. Fedor, and M. Allan, "Isotope effect in dissociative electron attachment to acetylene," Phys. Rev. A **80**, 012706 (2009).
[38]M. Fogle, D. J. Haxton, A. L. Landers, A. E. Orel, and T. N. Rescigno, "Ion-momentum imaging of dissociative-electron-attachment dynamics in acetylene," Phys. Rev. A **90**, 042712 (2014).
[39]R. Janečková, D. Kubala, O. May, J. Fedor, and M. Allan, "Experimental evidence on the mechanism of dissociative electron attachment in formic acid," Phys. Rev. Lett. **111**, 213201 (2013).
[40]M. Zawadzki, M. Čížek, K. Houfek, R. Čurík, M. Ferus, S. Civiš, J. Kočišek, and J. Fedor, "Resonances and dissociative electron attachment in HNCO," Phys. Rev. Lett. **121**, 143402 (2018).
[41]T. P. Ragesh Kumar, J. Kočišek, K. Bravaya, and J. Fedor, "Electron-induced vibrational excitation and dissociative electron attachment in methyl formate," Phys. Chem. Chem. Phys. **22**, 518 (2020).
[42]P. Nag, M. Tarana, and J. Fedor, "Effects of π^*–σ^* coupling on dissociative-electron-attachment angular distributions in vinyl, allyl, and benzyl chloride and in chlorobenzene," Phys. Rev. A **103**, 032830 (2021).
[43]S. Gulania and A. I. Krylov, "Dissociative electron attachment in C_2H via electronic resonances," Mol. Phys. **119**, e1979262 (2021).
[44]T. Sommerfeld and M. Ehara, "Complex absorbing potentials with Voronoi isosurfaces wrapping perfectly around molecules," J. Chem. Theory Comput. **11**, 4627 (2015).
[45]T.-C. Jagau, D. Zuev, K. B. Bravaya, E. Epifanovsky, and A. I. Krylov, "A fresh look at resonances and complex absorbing potentials: Density matrix based approach," J. Phys. Chem. Lett. **5**, 310 (2014).
[46]D. Zuev, T.-C. Jagau, K. B. Bravaya, E. Epifanovsky, Y. Shao, E. Sundstrom, M. Head-Gordon, and A. I. Krylov, "Complex absorbing potentials within EOM-CC family of methods: Theory, implementation, and benchmarks," J. Chem. Phys. **141**, 024102 (2014).
[47]N. Moiseyev, "Quantum theory of resonances: Calculating energies, widths and cross-sections by complex scaling," Phys. Rep. **302**, 212 (1998).
[48]N. Moiseyev and C. Corcoran, "Autoionizing states of H_2 and H_2^- using the complex-scaling method," Phys. Rev. A **20**, 814 (1979).
[49]B. Simon, "The definition of molecular resonance curves by the method of exterior complex scaling," Phys. Lett. A **71**, 211 (1979).
[50]S. Gozem and A. I. Krylov, "The ezSpectra suite: An easy-to-use toolkit for spectroscopy modeling," WIREs: Comput. Mol. Sci. **12**, e1546 (2022).
[51]Depending on molecular orientation, symmetry labels corresponding to the same orbital or vibrational mode may be different. Q-Chem's standard molecular orientation is different from that of Mulliken.[52] For example, Q-Chem would place a water molecule in the *xz* plane instead of the *yz* plane. Consequently, for C_{2v} symmetry, b_1 and b_2 labels are flipped. More details can be found at http://iopenshell.usc.edu/resources/howto/symmetry/. To avoid confusion with different molecular orientations and relabeling the states, here we report the structures and symmetry labels following Q-Chem's notations.
[52]R. S. Mulliken, "Report on notation for the spectra of polyatomic molecules," J. Chem. Phys. **23**, 1997 (1955).
[53]W. Skomorowski, S. Gulania, and A. I. Krylov, "Bound and continuum-embedded states of cyanopolyyne anions," Phys. Chem. Chem. Phys. **20**, 4805 (2018).
[54]Z. Benda and T.-C. Jagau, "Communication: Analytic gradients for the complex absorbing potential equation-of-motion coupled-cluster method," J. Chem. Phys. **146**, 031101 (2017).
[55]Z. Benda and T.-C. Jagau, "Understanding processes following resonant electron attachment: Minimum-energy crossing points between anionic and neutral potential energy surfaces," J. Chem. Theory Comput. **14**, 4216 (2018).
[56]A. T. B. Gilbert, N. A. Besley, and P. M. W. Gill, "Self-consistent field calculations of excited states using the maximum overlap method (MOM)," J. Phys. Chem. A **112**, 13164 (2008).
[57]P. Wójcik, S. Gozem, V. A. Mozhayskiy, and A. I. Krylov, "ezFCF (formerly ezSpectrum)," http://iopenshell.usc.edu/downloads/.
[58]A. I. Krylov and P. M. W. Gill, "Q-Chem: An engine for innovation," WIREs Comput. Mol. Sci. **3**, 317 (2013).
[59]E. Epifanovsky, A. T. B. Gilbert, X. Feng, J. Lee, Y. Mao, N. Mardirossian, P. Pokhilko, A. F. White, M. P. Coons, A. L. Dempwolff, Z. Gan, D. Hait, P. R. Horn, L. D. Jacobson, I. Kaliman, J. Kussmann, A. W. Lange, K. U. Lao, D. S. Levine, J. Liu, S. C. McKenzie, A. F. Morrison, K. D. Nanda, F. Plasser, D. R. Rehn, M. L. Vidal, Z.-Q. You, Y. Zhu, B. Alam, B. J. Albrecht, A. Aldossary, E. Alguire, J. H. Andersen, V. Athavale, D. Barton, K. Begam, A. Behn, N. Bellonzi, Y. A. Bernard, E. J. Berquist, H. G. A. Burton, A. Carreras, K. Carter-Fenk, R. Chakraborty, A. D. Chien, K. D. Closser, V. Cofer-Shabica, S. Dasgupta, M. de Wergifosse, J. Deng, M. Diedenhofen, H. Do, S. Ehlert, P.-T. Fang, S. Fatehi, Q. Feng, T. Friedhoff, J. Gayvert, Q. Ge, G. Gidofalvi, M. Goldey, J. Gomes, C. E. González-Espinoza, S. Gulania, A. O. Gunina, M. W. D. Hanson-Heine, P. H. P. Harbach, A. Hauser, M. F. Herbst, M. Hernández Vera, M. Hodecker, Z. C. Holden, S. Houck, X. Huang, K. Hui, B. C. Huynh, M. Ivanov, Á. Jász, H. Ji, H. Jiang, B. Kaduk, S. Kähler, K. Khistyaev, J. Kim, G. Kis, P. Klunzinger, Z. Koczor-Benda, J. H. Koh, D. Kosenkov, L. Koulias, T. Kowalczyk, C. M. Krauter, K. Kue, A. Kunitsa, T. Kus, I. Ladjánszki, A. Landau, K. V. Lawler, D. Lefrancois, S. Lehtola, R. R. Li, Y.-P. Li, J. Liang, M. Liebenthal, H.-H. Lin, Y.-S. Lin, F. Liu, K.-Y. Liu, M. Loipersberger, A. Luenser, A. Manjanath, P. Manohar, E. Mansoor, S. F. Manzer, S.-P. Mao, A. V. Marenich, T. Markovich, S. Mason, S. A. Maurer, P. F. McLaughlin, M. F. S. J. Menger, J.-M. Mewes, S. A. Mewes, P. Morgante, J. W. Mullinax, K. J. Oosterbaan, G. Paran, A. C. Paul, S. K. Paul, F. Pavošević, Z. Pei, S. Prager, E. I. Proynov, Á. Rák, E. Ramos-Cordoba, B. Rana, A. E. Rask, A. Rettig, R. M. Richard, F. Rob, E. Rossomme, T. Scheele, M. Scheurer, M. Schneider, N. Sergueev, S. M. Sharada, W. Skomorowski, D. W. Small, C. J. Stein, Y.-C. Su, E. J. Sundstrom, Z. Tao, J. Thirman, G. J. Tornai, T. Tsuchimochi, N. M. Tubman, S. P. Veccham, O. Vydrov, J. Wenzel, J. Witte, A. Yamada, K. Yao, S. Yeganeh, S. R. Yost, A. Zech, I. Y. Zhang, X. Zhang, Y. Zhang, D. Zuev, A. Aspuru-Guzik, A. T. Bell, N. A. Besley, K. B. Bravaya, B. R. Brooks, D. Casanova, J.-D. Chai, S. Coriani, C. J. Cramer, G. Cserey, A. E. DePrince, R. A. DiStasio, A. Dreuw, B. D. Dunietz, T. R. Furlani, W. A. Goddard, S. Hammes-Schiffer, T. Head-Gordon, W. J. Hehre, C.-P. Hsu, T.-C. Jagau, Y. Jung, A. Klamt, J. Kong, D. S. Lambrecht, W. Liang, N. J. Mayhall, C. W. McCurdy, J. B. Neaton, C. Ochsenfeld, J. A. Parkhill, R. Peverati, V. A. Rassolov, Y. Shao, L. V. Slipchenko, T. Stauch, R. P. Steele, J. E. Subotnik, A. J. W. Thom, A. Tkatchenko, D. G. Truhlar, T. Van Voorhis, T. A. Wesolowski, K. B. Whaley, H. L. Woodcock, P. M. Zimmerman, S. Faraji, P. M. W. Gill, M. Head-Gordon, J. M. Herbert, and A. I. Krylov, "Software for the frontiers of quantum chemistry: An overview of developments in the Q-Chem 5 package," J. Chem. Phys. **155**, 084801 (2021).
[60]M. Allan, "Measurement of differential cross sections for excitation of helium by electron impact within the first 4 eV above threshold," J. Phys. B: At., Mol. Opt. Phys. **25**, 1559 (1992).
[61]M. Allan, "Measurement of the elastic and $v = 0 \rightarrow 1$ differential electron–N_2 cross sections over a wide angular range," J. Phys. B: At., Mol. Opt. Phys. **38**, 3655 (2005).
[62]I. I. Fabrikant, "Long-range effects in electron scattering by polar molecules," J. Phys. B: At., Mol. Opt. Phys. **49**, 222005 (2016).
[63]M. A. Fennimore and S. Matsika, "Core-excited and shape resonances of uracil," Phys. Chem. Chem. Phys. **18**, 30536 (2016).
[64]M. Thodika, N. Mackouse, and S. Matsika, "Description of two-particle one-hole electronic resonances using orbital stabilization methods," J. Phys. Chem. A **124**, 9011 (2020).
[65]V. K. Voora and K. D. Jordan, "Nonvalence correlation-bound anion state of C_6F_6: Doorway to low-energy electron capture," J. Phys. Chem. A **118**, 7201 (2014).
[66]Y. Liu, G.-Z. Zhu, D.-F. Yuan, C.-H. Qian, Y.-R. Zhang, B. M. Rubenstein, and L.-S. Wang, "Observation of a symmetry-forbidden excited quadrupole-bound state," J. Am. Chem. Soc. **142**, 20240 (2020).
[67]T.-C. Jagau, D. B. Dao, N. S. Holtgrewe, A. I. Krylov, and R. Mabbs, "Same but different: Dipole-stabilized shape resonances in CuF^- and AgF^-," J. Phys. Chem. Lett. **6**, 2786 (2015).

[68]U. Nygaard, J. T. Nielsen, J. Kirchheiner, G. Maltesen, J. Rastrup-Andersen, and G. O. Sørensen, "Microwave spectra of isotopic pyrroles. Molecular structure, dipole moment, and ^{14}N quadrupole coupling constants of pyrrole," J. Mol. Struct. **3**, 491 (1969).
[69]T.-C. Jagau and A. I. Krylov, "Complex absorbing potential equation-of-motion coupled-cluster method yields smooth and internally consistent potential energy surfaces and lifetimes for molecular resonances," J. Phys. Chem. Lett. **5**, 3078 (2014).
[70]H. Hotop, M.-W. Ruf, M. Allan, and I. I. Fabrikant, "Resonance and threshold phenomena in low-energy electron collisions with molecules and clusters," *Advances in Atomic, Molecular, and Optical Physics* (Academic Press, 2003), Vol. 49, pp. 85–216.
[71]W. Domcke and C. Mündel, "Calculation of cross sections for vibrational excitation and dissociative attachment in HCl and DCl beyond the local-complex-potential approximation," J. Phys. B: At., Mol. Opt. Phys. **18**, 4491 (1985).
[72]T. Skalický and M. Allan, "The assignment of dissociative electron attachment bands in compounds containing hydroxyl and amino groups," J. Phys. B: At., Mol. Opt. Phys. **37**, 4849 (2004).
[73]M. V. Muftakhov, N. L. Asfandiarov, and V. I. Khvostenko, "Resonant dissociative attachment of electrons to molecules of five-membered heterocyclic compounds and lactams," J. Electron Spectrosc. Relat. Phenom. **69**, 165 (1994).
[74]C. S. Anstöter, G. Mensa-Bonsu, P. Nag, M. Ranković, Ragesh Kumar T. P., A. N. Boichenko, A. V. Bochenkova, J. Fedor, and J. R. R. Verlet, "Mode-specific vibrational autodetachment following excitation of electronic resonances by electrons and photons," Phys. Rev. Lett. **124**, 203401 (2020).
[75]J. Dvořák, M. Ranković, K. Houfek, P. Nag, R. Čurík, J. Fedor, and M. Čížek, "Vibronic coupling through the continuum in the e + CO_2 system," Phys. Rev. Lett. **129**, 013401 (2022).
[76]Ragesh Kumar T. P., P. Nag, M. Rankovič, T. F. M. Luxford, J. Kočišek, Z. Mašín, and J. Fedor, "Coupling of distant parts of pyrrole molecule through virtual and resonant states," arXiv:2208.13539 (2022).
[77]Z. Benda, K. Rickmeyer, and T.-C. Jagau, "Structure optimization of temporary anions," J. Chem. Theory Comput. **14**, 3468 (2018).
[78]W. Vanroose, Z. Zhang, C. W. McCurdy, and T. N. Rescigno, "Threshold vibrational excitation of CO_2 by slow electrons," Phys. Rev. Lett. **92**, 053201 (2004).
[79]M. Allan, "Vibrational structures in electron–CO_2 scattering below the $^2\Pi_u$ shape resonance," J. Phys. B: At., Mol. Opt. Phys. **35**, L387 (2002).
[80]P. Nag, R. Čurík, M. Tarana, M. Polášek, M. Ehara, T. Sommerfeld, and J. Fedor, "Resonant states in cyanogen NCCN," Phys. Chem. Chem. Phys. **22**, 23141 (2020).
[81]M. Allan, M. Lacko, P. Papp, Š. Matejčík, M. Zlatar, I. I. Fabrikant, J. Kočišek, and J. Fedor, "Dissociative electron attachment and electronic excitation in $Fe(CO)_5$," Phys. Chem. Chem. Phys. **20**, 11692 (2018).
[82]T.-C. Jagau and A. I. Krylov, "Characterizing metastable states beyond energies and lifetimes: Dyson orbitals and transition dipole moments," J. Chem. Phys. **144**, 054113 (2016).
[83]W. Skomorowski and A. I. Krylov, "Real and imaginary excitons: Making sense of resonance wavefunctions by using reduced state and transition density matrices," J. Phys. Chem. Lett. **9**, 4101 (2018).